Grid Current Control Method Appling Active Damping for Three-level Flying Capacitor Inverter with Small LCL-Filter

Hiroki Watanabe
Dept. of Electrical, Electronics and Information Engineering
Nagaoka University of Technology
Nagaoka, Japan
hwatanabe@vos.nagaokaut.ac.jp

Jun-ichi Itoh
Dept. of Science of Technology Innovation
Nagaoka University of Technology
Nagaoka, Japan
itoh@vos.nagaokaut.ac.jp

***Abstract*—This paper proposes an active damping method in the grid current control for a three-level flying capacitor grid-tied inverter with high robustness against the grid impedance variation. The proposed active damping control expands the stability region by adjusting the updating period of the voltage reference in active damping. This paper also introduces the design criteria of the *LCL*-filter and feedback control design for the stabilization of the inverter system. Experimental results demonstrate the validity of the proposed current control method. The experimental result shows that the proposed control improved the stability of the flying capacitor inverter under grid impedance variations. Finally, a sinusoidal current waveform with a Total Harmonic Distortion (THD) of less than 5% was obtained.**

Keywords—grid-tied inverter, LCL-filter, active damping, Nyquist frequency, multi-level inverter.

I. Introduction

Grid-tied Voltage Source Inverters (VSIs) have been widely employed for PV systems to deliver the generation power to a single or three-phase grid. In these systems, a harmonic filter, e.g., *LC* or *LCL*-filter, is necessary in the VSIs to eliminate the harmonic components [1]-[2]. The attenuation performance of the *LCL*-filter is better than that of the *LC*-filter despite the small filter inductor. However, the *LCL*-filter has a resonance pole, which causes the instability of power converter systems. Therefore, resonance damping is often considered in the converter design to improve the stability of these power electronics systems.

Passive and active damping methods have been considered to solve this problem. The passive damping attenuates the *LCL*-resonance by adding a damping resistor [3]-[4]. This damping method is a very simple solution to avoid the instability caused by the *LCL*-resonance. However, there is a trade-off between the converter loss and the damping performance of the damping resistor. The active damping method achieves resonance damping without any damping resistor. Active damping is implemented into the grid current control, which behaves as a virtual impedance in the closed loop.

Various active damping techniques have been proposed [5]-[6]. In Ref. [5], the stability of a system with active damping based on the proportional capacitor current feedback was discussed. The performance of the active damping with the digital control delay, such as the sampling delay is evaluated [5]. In Ref. [6], a hybrid active damping control method with two active damping was proposed. The hybrid active damping changes the damping method depending on the grid impedance variation to ensure the phase margin of the current control.

On the other hand, the high switching frequency operation with wide-band-gap devices of SiC and GaN contributes to the miniaturization of the harmonic filter owing to the increase of the cut-off frequency [7]-[9]. In the circuit topology, multi-level inverters are a better solution than two-level VSI because the multi-level inverter provides several voltage levels in the inverter output voltage to reduce the harmonic components. Generally, the resonance frequency of the harmonic filter is designed to be less than the Nyquist frequency to avoid resonance due to switching frequency components. However, this condition may limit the degree of freedom for the filter design. Design criteria of VSI with the high resonance frequency harmonic filter beyond the Nyquist frequency have been considered in Ref. [10]. However, this analysis is considered based on the constant grid impedance condition. The grid impedance may vary in the actual system due to the grid condition.

This paper proposes a current control method with active damping against the high *LCL*-resonance frequency beyond the Nyquist frequency. The proposed active damping is implemented based on the capacitor current feedback to attenuate the *LCL*-resonance. The contribution of this paper is that the proposed control method is highly robust against grid impedance variation. This paper introduces the details of the proposed control method, design criteria of the *LCL*-filter, and experimental results to confirm the validity of the proposed active damping method.

II. Circuit Configuration

A. Three-level Flying Capacitor Inverter

Fig. 1 shows the circuit configuration of a three-level flying capacitor inverter. The flying capacitor voltage is half of the DC-link voltage to increase the voltage level of the output voltage. The *LCL*-filter is connected to the inverter output side to attenuate the switching harmonics.

The inverter is connected to the single-phase grid through the Point of Common Coupling (PCC). The grid side includes the grid inductance L_g, which influences the *LCL*-resonance because the filter inductor impedance L_f becomes close to the impedance L_g when the *LCL*-resonance frequency increases.

B. *Capacitor Current Feedback-Based Active Damping*

Fig. 2 shows the block diagram of the grid current feedback control with the capacitor-current feedback-based active damping. The inner loop corresponds to the active damping based on the capacitor current feedback. The damping effect is provided by the damping gain K_t. The outer loop with controller $G_c[z]$ provides the current control to synchronize the current phase to the grid voltage for grid-tied operation.

Firstly, the transfer function from the inverter output voltage to the grid current is delivered to discuss the frequency characteristics of the feedback control. The transfer function is expressed as

$$G_{v_O \to i_g}[z] = \frac{1}{L+L_f+L_g}\left[\frac{T_s}{z-1} - \frac{1}{\omega_r}\frac{(z-1)\sin\omega_r T_s}{z^2-2z\cos\omega_r T_s+1}\right] \quad (1)$$

where L and L_f are the inductance of the *LCL*-filter, L_g is the grid side inductance, and T_s is the sampling time of the controller.

The *LCL*-resonance angular frequency of the *LCL*-filter is expressed as

$$\omega_r = 2\pi f_r = \sqrt{\frac{L+L_f+L_g}{L(L_f+L_g)C_f}} \quad (2)$$

where ω_r is the resonance angular frequency, f_r is the resonance frequency, and C_f is the filter capacitance. Usually, the filter inductance L_f is designed to be larger than the grid inductance L_g. However, L_g influences the *LCL*-resonance angular frequency when L_f is designed to be small for miniaturization.

Fig. 3 shows the open-loop frequency characteristics of the current control without active damping. Note that the *LCL*-resonance frequency is beyond the Nyquist frequency. In this case, the resonance frequency f_r^{image} caused by aliasing appears within the Nyquist frequency. f_r^{image} is expressed as

$$f_r^{\text{image}} = f_s - f_r \quad (3)$$

where f_s is the sampling frequency. According to Fig.3, the unstable region is from 1/6 of the sampling frequency due to the *LCL*-resonance [12].

Fig. 4 shows the control block diagram of the capacitor-current-feedback-based active damping control. Note that $G_d(s)$ is the delay, which includes the PWM delay. The active damping behaves as a virtual impedance connected in parallel to the filter capacitor as shown in Fig.4. The virtual impedance is expressed as

$$Z_{AD}(\omega) = \frac{L}{K_t C_f \cos(0.5+\lambda)\omega T_s} \quad (4)$$

where λ is the calculation delay of the renewal of the voltage command from the sampling instant, K_t is the damping gain, and C_f is the filter capacitor.

III. Proposed Active Damping Control

Fig. 5 shows the control block diagram of the current control with the proposed active damping. In the proposed control, the AD conversion and output timing of the outer loop are synchronized with the top of the triangular carrier of the inverter as shown in Fig. 5 (b). In this case, the voltage command for the current control has a delay of one sampling period. The output timing of the inner loop is set at the bottom of the triangular carrier. In this case, the sampling delay becomes half the sampling period compared to the outer loop. In addition, the inner loop provides positive feedback through the negative damping gain. Furthermore, phase-lag compensation is added to extend the phase margin. The transfer function between the inverter output voltage v_o and the filter capacitor current i_c is obtained from the control block diagram in Fig. 6. It is expressed as

$$G_{v_O \to i_C}[z, m=0.5] = \frac{\sin 0.5\omega_r T_s}{\omega_r L}\frac{z^2-1}{z(z^2-2z\cos\omega_r T_s+1)} \quad (5)$$

where m means 1 - λ. The transfer function of the phase delay compensator is obtained using the bilinear transform. It is expressed as

$$G_{AD}[z] = K_t\frac{(1+b)z+(1-b)}{(1+a)z+(1-a)} \quad (6)$$

$$\begin{cases} a = \dfrac{1}{b}A \\ b = B+\sqrt{B^2+A} \\ A = \dfrac{1+\cos\omega_{\max}T_s}{1-\cos\omega_{\max}T_s},\ B = \dfrac{(1+\cos\omega_{\max}T_s)\tan\phi_{\max}}{\sin\omega_{\max}T_s} \end{cases} \quad (7)$$

where $\omega_{\max}$ is the maximum angular frequency with maximum phase delay, and $\Phi_{\max}$ is the maximum phase of the phase-lag compensation.

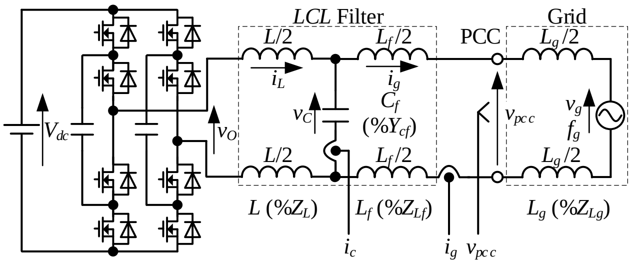

Fig. 1. Flying capacitor typed 3-level single-phase grid-tied inverter with *LCL* filter.

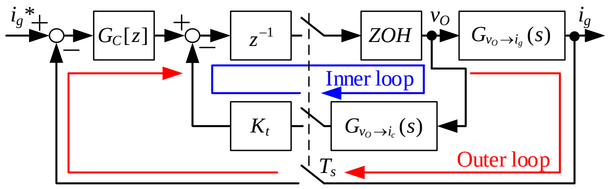

Fig. 2. Simplified block diagram of grid current feedback control with active damping method.

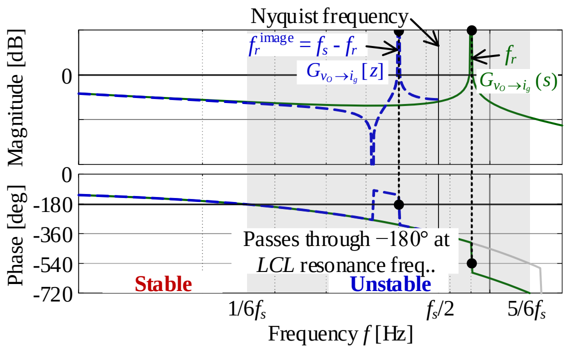

Fig. 3. Open-loop frequency characteristics of grid-tied inverter.

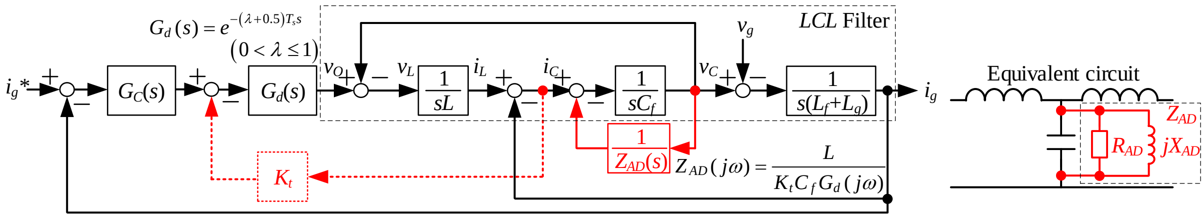

Fig. 4. Block diagram of conventional active damping method based on capacitor current feedback.

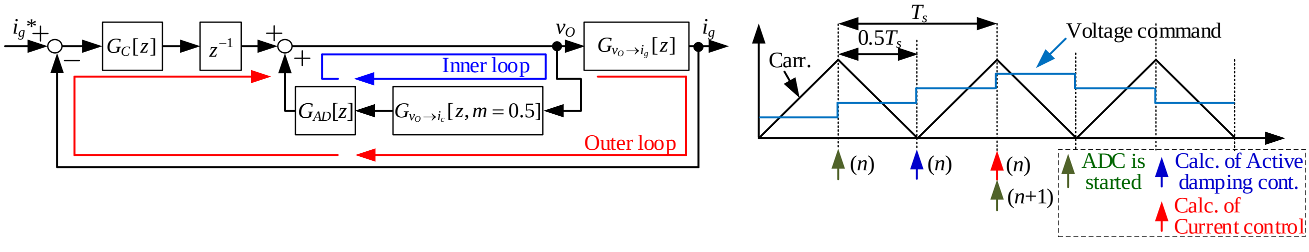

(a) Block diagram of current control. (b) Calculation timing of active damping and current control.

Fig. 5. Proposed grid current feedback control with active damping.

Fig. 6 shows the frequency characteristics of the virtual impedance calculated using (4). According to Fig.6, the virtual impedance becomes positive in the 1/2 < fr/fs < 5/6 region, which means the active damping provides a damping effect against the *LCL*-resonance. However, a negative impedance occurs in the 5/6 < fr/fs < 1 region, where it causes instability. Therefore, the stability region of this active damping method depends on the sampling frequency and *LCL*-resonance frequency.

Fig. 7 shows the frequency characteristics of the virtual impedance of the proposed active damping method. According to Fig. 7, the positive impedance is obtained when the range of f_r/f_s is 0.25 to 0.75, which means that the positive impedance region is extended by 50% compared to that for the conventional active damping method in Fig. 5.

Fig. 8 shows the open-loop Bode plot of the proposed active damping. As shown in Fig. 8, the gain margin g_m and phase margin p_m decrease when the ratio of f_r/f_s is 0.73. The stability margin is improved when the *LCL*-resonance is close to the Nyquist frequency. Thus, the stability margin should be improved when the *LCL*-resonance frequency is far from the Nyquist frequency. Therefore, phase-lag compensation is added to improve the phase margin. Improving the stability margin using phase-lag compensation is difficult in the conventional active damping method because its unstable region is close to the Nyquist frequency. In contrast, improving the stability margin for the proposed active damping method is possible because the compensation frequency is not close to the Nyquist frequency.

The design criteria for the proposed active damping method based on the stability margin are as follows. The open-loop transfer function of the proposed active damping is expressed as

$$T_{inner}[z] = G_{AD}[z] G_{v_O \to i_C}[z, m = 0.5] \tag{8}$$

where the transfer functions of $G_{vo\to ic}$ $[z,m = 0.5]$ and G_{AD} $[z]$ are obtained from (5) and (6), respectively. Note that the gain margin is the gain of $10^{(GM/20)}|T_{inner}[z = \exp(j\omega_{cp}T_s)]| = 1$ at the phase cross-over angular frequency ω_{cp} of $\angle T_{inner}[z = \exp(j\omega_{cp}T_s)] = \pi$. According to the phase-cross-over frequency, $\omega_{cp}T_s$ is expressed as

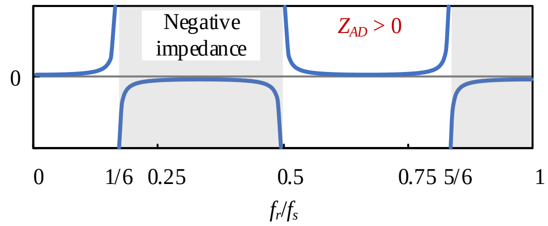

Fig. 6. Frequency characteristics of virtual impedance. ($\lambda = 1$, $K_t > 0$)

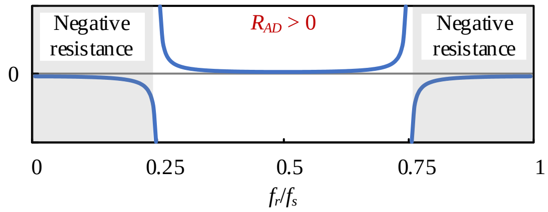

Fig. 7. Frequency characteristics of R_{AD} from (4). ($\lambda = 0.5$, $K_t < 0$)

$$\omega_{cp}T_s = \cos^{-1}\frac{-(1+ab)+\sqrt{(1+ab)^2+4(1+a)(1-b)(a-b)}}{2(1+a)(1-b)} \tag{9}$$

The maximum value of the damping gain based on the gain margin K_{t_GM} is obtained by (9) and a gain of $10^{(GM/20)}|T_{inner}[z = \exp(j\omega_{cp}T_s)]| = 1$. K_{t_GM} is expressed as

$$K_{t\_GM} = 10^{-\frac{GM}{20}} \cdot \omega_r L \sqrt{\frac{1+a^2\tan^2 0.5\omega_{cp}T_s}{1+b^2\tan^2 0.5\omega_{cp}T_s}} \left|\frac{\cos\omega_{cp}T_s - \cos\omega_r T_s}{\sin 0.5\omega_r T_s \sin\omega_{cp}T_s}\right| \tag{10}$$

The maximum value of the damping gain is calculated based on the phase margin Kt_PM. According to the derivation of K_{t_GM}, $|T_{inner}[z = \exp(j\omega_{cg}T_s)]| = 1$. Therefore, K_{t_PM} is given by

$$K_{t\_PM} = \omega_r L \sqrt{\frac{1+a^2\tan^2 0.5\omega_{cg}T_s}{1+b^2\tan^2 0.5\omega_{cg}T_s}} \left|\frac{\cos\omega_{cg}T_s - \cos\omega_r T_s}{\sin 0.5\omega_r T_s \sin\omega_{cg}T_s}\right| \tag{11}$$

Note that the gain cross-over angular frequency is obtained by solving the following equation:

$$\frac{(b-a)\sin\omega_{cg}T_s\tan\left(PM-\omega_{cg}T_s\right)}{(1+ab)+(1-ab)\cos\omega_{cg}T_s}=1 \qquad (12).$$

Note that this equation has a solution when the following condition is satisfied:

$$0<\omega_{cg}T_s<\frac{\pi}{2}+PM \qquad (13).$$

The gain cross-over frequency is calculated from (12) using the iterative method. According to (8) to (12), the damping gain K_t that satisfies both the gain and phase margin is given by

$$K_t=\min\left(K_{t\_GM},K_{t\_PM}\right) \qquad (14).$$

Fig. 9 shows the open-loop Bode plot of the proposed active damping method with phase-lag compensation. Note that the gain margin is designed to be 3 dB, and the phase margin is designed to be 30°. According to Fig. 9, the phase margin increases when the phase-lag compensation is applied.

Fig. 10 shows the open-loop Bode plot of the current control. The open loop transfer function of the current control is expressed as

$$T_{outer}[z]=\frac{G_C[z]z^{-1}G_{v_O\to i_g}[z]}{1+G_{AD}[z]G_{v_O\to i_C}[z,m=0.5]} \qquad (15).$$

According to Fig. 10, the peak gain of the *LCL*-resonance decreases compared to that obtained without active damping. However, the peak gain of the *LCL*-resonance is still on the green line because the loop gain is low due to the limitation of the stability margin.

The peak gain *LCL*-resonance drastically decreases due to the addition of phase-lag compensation because the loop gain becomes higher than that obtained without.

IV. Design Criteria of LCL-filter and Controller

The inverter-side-filter inductor on the *LCL*-filter is designed based on the current ripple. The filter capacitor and the grid-side-filter inductor are designed based on the resonance frequency. Note that the *LCL*-resonance frequency depends on the grid impedance. The filter capacitor and the grid-side-filter inductor are respectively designed as

$$C_f=\frac{1}{L\left(2\pi f_{r\_weak}\right)^2} \qquad (16)$$

$$L_f=\frac{L}{\left(2\pi f_{r\_stiff}\right)^2LC_f-1}=\frac{L}{\left(f_{r\_stiff}/f_{r\_weak}\right)^2-1} \qquad (17)$$

where f_{r_stiff} is the *LCL*-resonance frequency for the stiff grid condition, and f_{r_weak} is for the weak grid condition.

The proposed current control adopts the proportional Resonance (PR) controller. The transfer function of the PR controller is expressed as

$$G_C(s)=K_p\left(1+\frac{1}{T_r}\frac{2\omega_i s}{s^2+2\omega_i s+\omega_o^2}+\frac{1}{T_r}\frac{2\omega_i s}{s^2+2\omega_i s+(5\omega_o)^2}\right) \qquad (18)$$

where K_p is the proportional gain, T_r is the resonance time, ω_i is the resonance angular frequency width, and ω_o is the resonance angular frequency. Note that the resonance angular frequency is set to the grid angular frequency. In addition, the resonance angular frequency width is set to 1% of the grid angular frequency. K_p and T_r are respectively expressed as

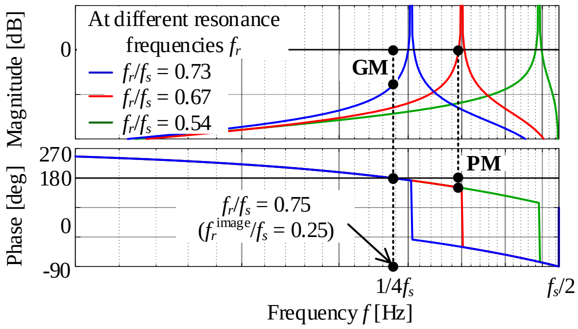

Fig. 8. Inner-loop frequency characteristics with capacitor-current positive feedback with reduced computation delay.

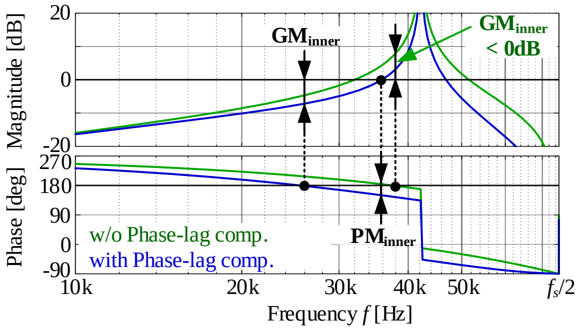

Fig. 9. Inner-loop frequency characteristics with or w/o phase lag compensator.

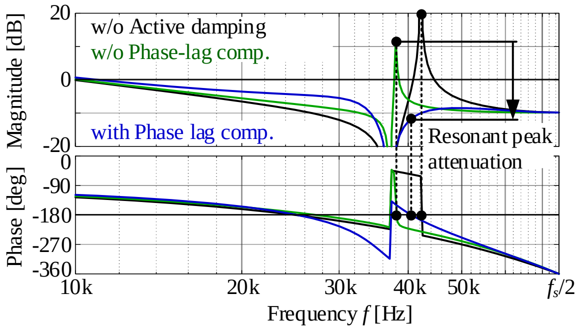

Fig. 10. Open-loop frequency characteristics of outer-loop.

$$K_p\cong\omega_c\left(L+L_f\right) \qquad (19)$$

$$T_r=\frac{2\omega_i\omega_c}{\tan\left(PM+1.5\omega_cT_s-\frac{\pi}{2}\right)}\cdot\left(\frac{1}{\omega_o^2-\omega_c^2}+\frac{1}{(5\omega_o)^2-\omega_c^2}\right) \qquad (20).$$

Table I shows the system parameters designed (15) to (19). In this paper, the robustness of the grid-tied inverter is evaluated using a grid impedance variation rate of 10%.

Fig. 11 shows the open-loop Bode plot of the current control with the proposed active damping method, and Fig. 12 shows the root locus with the grid impedance variation. According to Fig. 11, the stability margin satisfies the stability condition. The phase margin for the stiff grid condition is improved owing to the phase-lag compensation. According to Fig. 12, the proposed current control satisfies the stability conditions due to the phase-lag compensation.

V. Experimental Results

Fig. 13 shows the experimental results for the proposed current control with the stiff and weak grid conditions. According to Fig. 13, a sinusoidal current waveform with low

Total Harmonic Distortion (THD) less than 5% is obtained under both conditions. In addition, the five-level voltage is also obtained owing to the flying-capacitor multi-level inverter. It confirmed that the fundamental operation of the proposed control.

Fig. 14 shows the experimental results of the steady-state operation with or without active damping control. According to Fig. 14 (a), the *LCL*-resonance occurs when the active damping control is disabled. The proposed active damping effectively suppresses the LCL-resonance under the stiff grid condition.

According to Fig. 14 (b), the *LCL*-resonance does not occur without active damping. This is because the parasitic capacitor of the MOSFETs and the dead time damps the *LCL*-resonance. This attenuation appears for both the weak grid and the stiff grids. However, the *LCL*-resonance is not sufficiently damped due to the current control's high loop gain under the stiff grid condition.

Fig.15 shows the experimental waveforms of the transient operation with active damping. As shown in Fig.15, the grid current is still stable during the transient behavior owing to the active damping control.

VI. Conclusion

This paper proposed a current control method with active damping control with a wide damping region for grid-tied inverters with a very small *LCL*-filter. The proposed active damping ensures stability under a very small *LCL*-filter less than 0.1% of unit impedance at a high resonance frequency beyond the Nyquist frequency. Furthermore, the design criteria of the *LCL*-filter and the controller were given the hardware and software design. The stability analysis results clarified the influence of the grid impedance variation. The experimental results for a 1 kW prototype confirmed the validity of the proposed control. As the experimental result, it was confirmed that the proposed control was stable under grid impedance variations. Finally, the sinusoidal current waveform with THD was obtained in less than 5% of the cases.

References

[1] X. Wang, F. Blaabjerg, and W. Wu, "Modeling and Analysis of Harmonic Stability in an AC Power-Electronics-Based Power System" *IEEE trans. Power Electron.*, vol.29, no.12, pp.6421-6432, Dec. 2014.

[2] D. Pan, X. Ruan, C. Bao, W. Li, and X. Wang, "Optimized Controller Design for LCL-Type Grid-Connected Inverter to Achieve High Robustness Against Grid-Impedance Variation" *IEEE trans. Ind. Electron.*, vol.62, no.3, pp.1537-1547, Mar. 2015.

[3] W. Wu, Y. He, T. Tang, and F. Blaabjerg, "A New Design Method for the Passive Damping LCL and LLCL Filter-Based Single-Phase Grid-Tied Inverter" *IEEE trans. Ind. Electron.*, vol. 60, no.10, pp.4339-4350, Oct. 2013.

[4] W. Wu, Y. Liu, Y. He, H. Chung, M. Liserre, and F. Blaabjerg, "Damping Methods for Resonances Caused by LCL-Filter-Based Current-Controlled Grid-Tied Power Inverters: An Overview" *IEEE trans. Ind. Electron.*, vol.64, no.9, pp.7402-7413, Sept. 2017.

[5] Z. Ma, L. Zhou, and J. Liu, "Proportional Capacitor Current Feedback Based Active Damping Control for LCL-Filter Converters with Considerable Control Delay" *IEEE Appl. Power Electron. Conf. Expo.*, pp.3110-3114, Mar. 2020.

[6] X. Wang, Q. Yang, H. Qing, and C. Zhang, Hybrid Active Damping Control Method for Grid Connected LCL Inverters Under Weak Grid" *IEEE Int. Power Electron. Appl. Conf. Expo.*, Nov. 2018.

Table I System Parameters

Symbol	Quantity	Value
V_{dc}	DC-link Voltage	350 V
V_g	Grid Voltage	200 V_{rms}
P_n	Nominal Power	1 kW
f_g	Grid Frequency	50 Hz
Z_b	Base Impedance	40 Ω
C_b	Base Capacitance	79.6 μF
	Switching Device	SCT3030AL (ROHM)
N	Number of Level	3
f_{sw}	Switching Frequency	150 kHz
f_{eq_sw}	Equivalent Switching Freq.	600 kHz
L	Inductor (%Z_L = 0.048%)	61 μH
C_f	Filter Capacitor (%Y_{Cf}=0.088%)	0.07 μF
L_f	Filter Inductor (%Z_{Lf} = 0.048%)	61 μH
f_{r_stiff}	*LCL* Resonance Frequency	108.9 kHz
f_{r_weak}	*LCL* Resonance Frequency	77 kHz
f_s	Sampling Frequency	150 kHz
f_c	Crossover Frequency	10 kHz
PM	Phase Margin	45 deg.
K_p	Proportional Gain	7.67 Ω
T_r	Resonance Period	1.26 ms
f_i	Resonance Frequency Width	0.5 Hz
ϕ_{max}	Maximum Phase of Lag comp.	-36.6 deg.
K_t	Damping Gain	-23.73 Ω

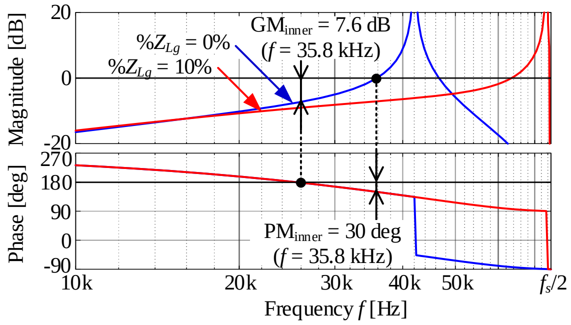

(a) Inner-loop frequency characteristics.

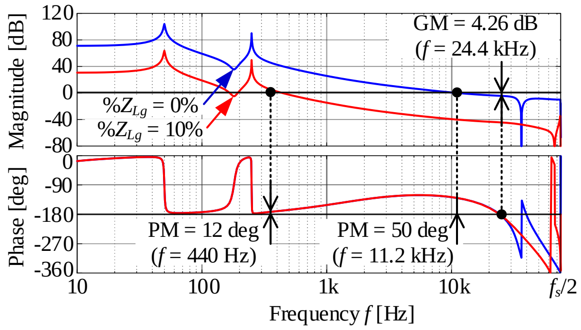

(b) Outer-loop frequency characteristics.

Fig. 11. Inner and outer loop characteristics.

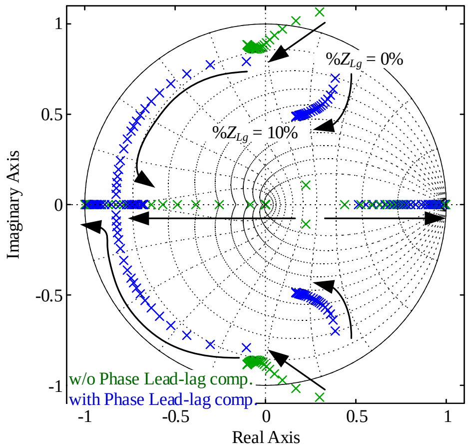

Fig. 12. Root locus of proposed current control.

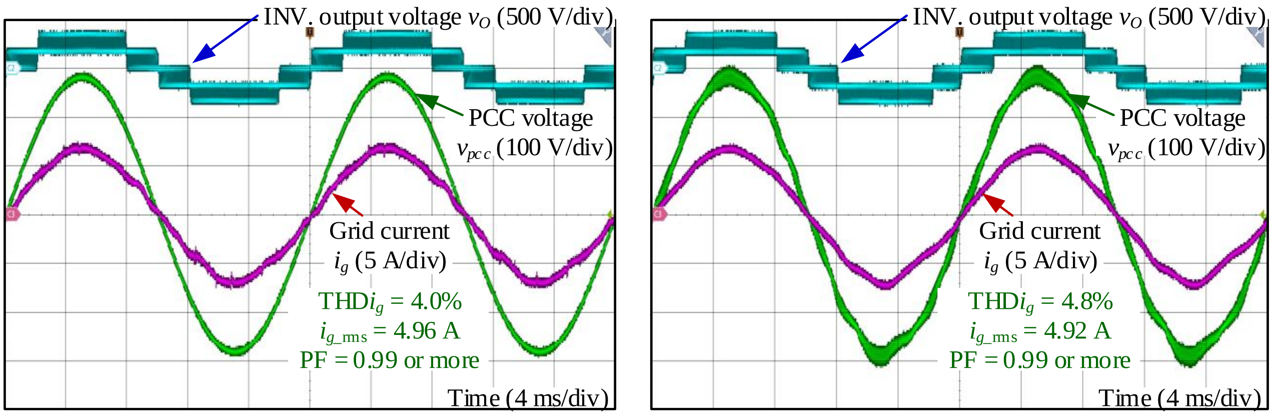

(a) Stiff grid at $\%Z_g$ = 0% (L_g = 0 mH) (b) Weak grid at $\%Z_g$ = 10% (L_g = 12.7 mH)

Fig. 13. Steady-state operation waveforms with proposed active damping.

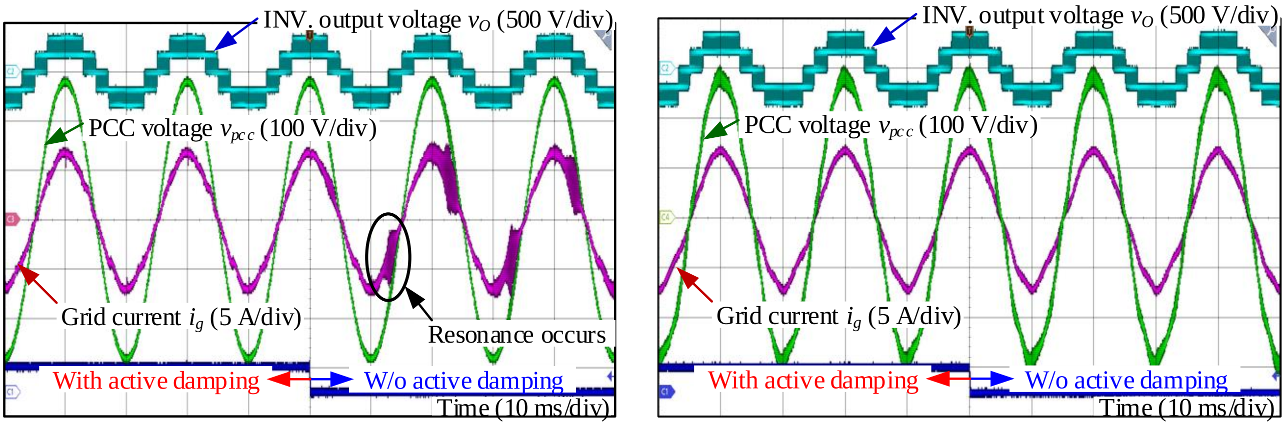

(a) Stiff grid at $\%Z_g$ = 0% (L_g = 0 mH) (b) Weak grid at $\%Z_g$ = 10% (L_g = 12.7 mH)

Fig. 14. Steady-state operation with or without the proposed active damping control.

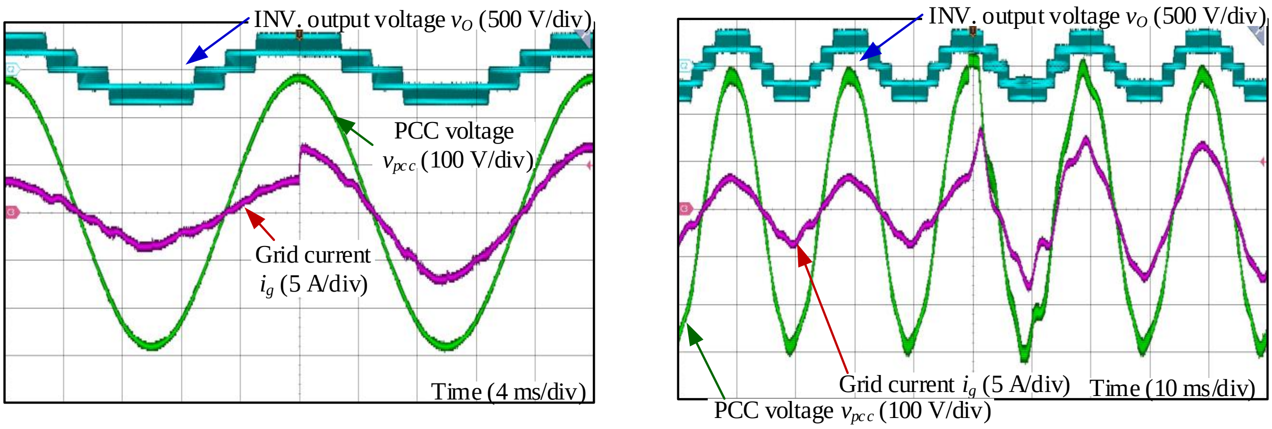

(a) Stiff grid at $\%Z_g$ = 0% (L_g = 0 mH). (b) Weak grid at $\%Z_g$ = 10% (L_g = 12.7 mH).

Fig. 15. Transient waveforms with proposed active damping.

[7] S. Nagai, K. Kusaka, and J. Itoh, "ZVRT Capability of Single-Phase Grid-Connected Inverter With High-Speed Gate-Block and Minimized LCL Filter Design" *IEEE trans. Ind. Appl.*, vol.54, no.5, pp.5387-5399, Sept. 2018.

[8] S. Nagai, and J. Itoh, "Open-Loop-Based Island-mode Voltage Control Method for Single-Phase Grid-tied Inverter with Minimized LC Filter" *IEEJ jour. Ind. Appl.*, vol.8, no.1, pp.108-115, Jan. 2019.

[9] Y. Tang, W. Yao, P. C. Loh, and F. Blaabjerg, "Design of LCL-filters with LCL resonance frequencies beyond the Nyquist frequency for grid-connected inverters" *IEEE Energy Conversion Congr. Expo.*, pp.5137-5144, Oct. 2015.

[10] L. Harnefors, R. Finger, X. Wang, H. Bai, and F. Blaabjerg, "VSC Input-Admittance Modeling and Above the Nyquist Frequency for Passivity-Based Stability Assessment" *IEEE trans. Ind. Electron.*, vol.64, no.8, pp.6362-6370, Aug. 2017